Chinese Chemical Letters 37 (2026) 112283

Contents lists available at ScienceDirect

Chinese Chemical Letters

journal homepage: www.elsevier.com/locate/cclet

Optimizing exciton interactions in covalent organic frameworks for boosting photocatalytic hydrogen peroxide production toward water decontamination

Jun Gao[a], Lichao Wang[a], Shunwei Huang[a], Hao Du[a], Huayue Zhu[b], Derek Hao[c], Yanling Wu[a,*], Qi Wang[a,*], Limin Jin[a,*]

[a] Zhejiang Key Laboratory of Solid Waste Pollution Control and Resource Utilization, School of Environmental Science and Engineering, Zhejiang Gongshang University, Hangzhou 310012, China
[b] Institute of Environmental Engineering Technology, Taizhou University, Taizhou 318000, China
[c] School of Science, RMIT University, Melbourne 3000, Australia

ARTICLE INFO

Article history:
Received 21 July 2025
Revised 10 October 2025
Accepted 14 December 2025
Available online 15 December 2025

Keywords:
Covalent organic frameworks
Donor-π-acceptor
Exciton binding energy
Photocatalytic H_2O_2 production
Water decontamination

ABSTRACT

Solar-driven hydrogen peroxide (H_2O_2) production presents a sustainable alternative to energy-intensive industrial methods, yet its efficiency using covalent organic frameworks (COFs) suffer from energy loss caused by strong exciton interactions. Herein, we designed COFs with donor-π-acceptor (D-π-A) architectures, using 2,5-dimethoxy-1,4-benzenedicarboxaldehyde as the D unit and optimizing the N-containing π-bridge units. The resulting TAPT–OCH_3 COF, incorporating 4,4′,4′′-(1,3,5-triazine-2,4,6-triyl)trianiline as the A unit, demonstrated the extended electron pathways and the reduced exciton recombination, markedly boosting photocatalytic performance. Experimental results revealed that TAPT–OCH_3 achieved a solar-to-chemical efficiency of 0.23 % and a quantum yield of 2.21 % at 420 nm, outperforming most reported COFs and metal-free catalysts. *In situ* characterization and theoretical calculations revealed that the TAPT–OCH_3 enhances charge separation to drive H_2O_2 production *via* a $2e^-$ oxygen reduction pathway, while its tailored electronic structure simultaneously improves the $1e^-$ water oxidation process. Crucially, TAPT–OCH_3 maintained high efficacy across diverse water sources and continuous-flow reactors under natural sunlight, enabling scalable H_2O_2 synthesis for water purification. Life cycle assessment confirmed the application stability of this material, underscoring its potential for sustainable environmental remediation. This work establishes a design paradigm for optimizing exciton dynamics in COF, highlighting the critical role of structural design for artificial H_2O_2 photosynthesis.

© 2026 Published by Elsevier B.V. on behalf of Chinese Chemical Society and Institute of Materia Medica, Chinese Academy of Medical Sciences.

Hydrogen peroxide (H_2O_2) has emerged as an eco-friendly chemical with broad applications spanning water purification, healthcare, and renewable energy systems [1]. Its appeal as an energy carrier stems from a high energy density (3.0 MJ/L), surpassing even compressed hydrogen (2.8 MJ/L at 35 MPa), while offering safer storage and transport [2]. Despite these benefits, conventional H_2O_2 production relies on the energy-intensive anthraquinone oxidation process, which demands costly noble metal catalysts, generates hazardous byproducts, and requires complex separation steps [3,4]. To address these limitations, sustainable alternatives such as electrocatalytic synthesis *via* the $2e^-$ oxygen reduction reaction (ORR) have gained traction, enabling on-demand H_2O_2 generation under ambient conditions [5,6]. However, practical challenges persist, such as low oxygen solubility in electrolytes, rapid H_2O_2 decomposition on metal-based catalysts, and the competing $4e^-$ ORR pathway for H_2O formation. These factors collectively limit industrial viability, often restricting operational currents to $<100\ mA/cm^2$ and minimal H_2O_2 yields <0.1 wt% [6,7]. While metal-free carbon catalysts offer a promising alternative, their adoption is hindered by unresolved questions about active site identification and design principles [8,9]. Thus, developing energy-efficient, cost-effective methods for H_2O_2 synthesis remains a pressing priority.

Artificial photosynthesis presents a compelling route, enabling sustainable H_2O_2 production from water and oxygen under sunlight [10–12]. Current approaches focus on the $2e^-$ ORR, which proceeds *via* single-step or two-step mechanisms [13,14]. However, natural water sources contain vastly more water molecules

* Corresponding authors.
E-mail addresses: wuyanling@zjgsu.edu.cn (Y. Wu), wangqi8327@zjgsu.edu.cn (Q. Wang), jinlimin@zjgsu.edu.cn (L. Jin).

https://doi.org/10.1016/j.cclet.2025.112283
1001-8417/© 2026 Published by Elsevier B.V. on behalf of Chinese Chemical Society and Institute of Materia Medica, Chinese Academy of Medical Sciences.

than dissolved oxygen (<10 mg/L), suggesting that enhancing water oxidation reactions (WOR) could substantially boost photocatalytic H_2O_2 yield [15]. According to previous reports, three primary WOR pathways exist: The $1e^-$ pathway generates hydroxyl radicals ($^{\bullet}OH$) that combine to form H_2O_2; the direct $2e^-$ pathway produce H_2O_2; and the $4e^-$ pathway yield oxygen for subsequent reduction to H_2O_2 [16–18]. The $1e^-$ pathway is particularly attractive, as it not only enables H_2O_2 formation but also supports $^{\bullet}OH$-driven applications like pollutant degradation. Yet, conventional inorganic semiconductors like TiO_2 exhibit poor efficiencies for H_2O_2 generation *via* WOR, with external quantum efficiencies below 1 % for $^{\bullet}OH$-mediated routes [19,20]. These limitations arise from material-reaction mismatches: The strong oxidative potentials of metal oxides (*e.g.*, ~3.0 V *vs.* NHE) and nitrides (~2.0 V) thermodynamically favor $4e^-$ or $2e^-$ pathways [21]. Balancing these thermodynamic factors is therefore critical to optimizing the $1e^-$ WOR pathway for efficient H_2O_2 production.

Recently, covalent organic frameworks (COFs) have gained increasing attention for controllable photocatalytic synthesis and decomposition of H_2O_2 due to their light-harvesting capabilities, customizable electronic properties, and abundant catalytic sites [22,23]. However, a fundamental challenge persists: Photogenerated electrons (e^-) and holes (h^+) in COFs recombine rapidly due to strong electrostatic attraction, leading to energy loss and lower catalytic efficiency [9,24]. To address this, researchers have focused on reducing the energy barrier for charge separation, known as exciton binding energy (E_b), by integrating donor-acceptor (D-A) units into COF backbones [25,26]. The electron push-pull interaction between D and A units promotes exciton dissociation and suppresses recombination, while enabling precise tuning of redox properties in facilitating the WOR and ORR pathway [27,28]. Despite these advances, structural imperfections in COFs, such as torsional strain in linear linkages, introduce large angles between D and A units, disrupting molecular planarity and impeding electron delocalization [29]. Thus, achieving high-performance COF photocatalysts requires not only functional frameworks but also precise alignment of energy levels between D-A components.

In this study, we present a straightforward and adaptable D-π-A structural extension strategy aimed to reduce E_b value in COFs materials, thereby enhancing the photocatalytic performance for H_2O_2 generation. By examining the impact of various D-π-A units on the coplanarity of the COFs, 2,5-dimethoxy-1,4-benzenedicarboxaldehyde serves as the D unit, while the A units are modulated through interconnection with 4,4′,4′′-(1,3,5-triazine-2,4,6-triyl)trianiline (TAPT–OCH_3), 1,3,5-tri(4-aminophenyl)benzene (TAPB–OCH_3), or tris(4-aminophenyl)amine (TAPA–OCH_3) as the A units, respectively. Among these, TAPT–OCH_3 exhibited significantly higher ORR and WOR activity, achieving a rate of 924 μmol g^{-1} h^{-1} from oxygen and water without sacrificial agents, with a notable apparent quantum yield (AQY) of 2.21 % at 420 nm and a superior solar-to-chemical conversion (SCC) efficiency of 0.23 %. For practical application, TAPT–OCH_3 was immobilized onto a continuous-flow reactor to consecutively produce H_2O_2, achieving *in-situ* disinfection of bacteria and degradation of organic contaminants in various real water samples. The strategic design of D-π-A structures presents a promising avenue for developing efficient low-E_b COF photocatalysts in future research.

To systematically examine how D and A units govern molecular geometry and electronic properties, a series of COFs with tailored D-A architectures were synthesized using varying monomers (Texts S1-S5 in Supporting information). As depicted in Figs. 1a-c, 2,5-dimethoxy-1,4-dialdehyde served as the D unit, leveraging its electron-donating methoxy groups to enhance π-electron delocalization. Complementary A units, TAPT featured an electron-deficient triazine core; TAPB and TAPA delocalized electron-deficient aromatic systems, were selected to induce controlled molecular torsion, optimizing electronic interactions for improved charge mobility and photocatalytic activity. Electrostatic potential (ESP) mapping (Figs. 1d-f) demonstrated that geometric isomerization amplifies dipole moments, enabling precise electronic redistribution. Dihedral angle analysis revealed structural variations: TAPT-OCH_3 exhibited near-planarity (70.2°), while TAPA-OCH_3 and TAPB-OCH_3 showed angles of 108.2° and 102.5°, respectively (Fig. S1 in Supporting information). The triazine π-bridge in TAPT-OCH_3 enhanced coplanarity, whereas the amine chains in TAPA-OCH_3 introduced rotational flexibility. The spatial separation in TAPT-OCH_3 calculated from the highest occupied and lowest unoccupied molecular orbitals (HOMO and LUMO) confirms the formation of a charge-transfer excited state (Fig. S2 in Supporting information). This observation was further supported by localized orbital locator (LOL-π) analysis, which highlighted extensive π-electron delocalization in TAPA-OCH_3, consistent with strong D-A coplanarity and efficient charge separation (Figs. 1g-i).

The crystallinity and structural parameters of the synthesized COFs were analyzed using powder X-ray diffraction (PXRD) and theoretical simulations [30]. The PXRD patterns of these samples exhibited sharp and similar peaks, indicating the high crystallinity and isostructural nature (Figs. 2a-c). Sharp, well-defined PXRD peaks confirmed the high crystallinity and isostructural nature of the three COFs. Distinct primary diffraction peaks at 2.84°, 2.89°, and 2.95° were observed for TAPT-OCH_3, TAPB-OCH_3, and TAPA-OCH_3, respectively, corresponding to the (100) crystallographic plane [31]. Additional peaks for the (110), (200), and (210) planes appeared at higher angles: 4.83°, 7.47°, and 9.51° for TAPT-OCH_3; 5.63°, 7.43°, and 9.74° for TAPB-OCH_3, while the (200) and (210) planes appeared at higher angles of 6.52° and 10.87° for TAPA-OCH_3 [32]. All samples displayed a broad peak near 25°, attributed to π-π stacking interactions between COF layers along the (001) plane [33]. Furthermore, the Pawley refinement of the PXRD data revealed detailed unit cell parameters. For TAPT–OCH_3, the refined lattice matched a honeycomb structure ($R_p = 1.74$ %, $R_{wp} = 1.35$ %) with unit cell dimensions of $a = 37.72$ Å, $b = 36.29$ Å, $c = 3.97$ Å, and angles $\alpha = \beta = 90°$, $\gamma = 120°$, consistent with the idealized AA-stacking configuration [30]. Similar refinements for TAPB–OCH_3 and TAPA-OCH_3 (Table S1 in Supporting information) confirmed analogous crystallographic parameters and atomic coordinates, supporting their *syn*-AA-stacked architectures. Based on the PXRD patterns and simulated stacking models, the hexagonal pore diameters of TAPT-OCH_3, TAPB-OCH_3, and TAPA-OCH_3 were calculated as 34.65, 34.35, and 30.34 Å, respectively (inset). The interlayer π-π stacking distances, derived from the (001) plane *d*-spacings, were 3.97 Å (TAPT–OCH_3), 3.75 Å (TAPB–OCH_3), and 4.13 Å (TAPA–OCH_3). These findings demonstrate that the three COFs possess well-defined crystalline structures and excellent crystallinity.

The surface morphology of the COFs was further examined using scanning electron microscopy (SEM). TAPT–OCH_3 presented a grass-like morphology consisting of well-bedded nanowires with diameters of 200 nm (Figs. 2d-f), while TAPB–OCH_3 and TAPA–OCH_3 displayed blocky structures composed of aggregated microspheres. The porosity and surface area of the as-synthesized COFs were further analyzed using N_2 adsorption-desorption isotherms [34]. As shown in Fig. 2g, Brunauer-Emmett-Teller (BET) surface area calculations revealed values of 1889.1, 1460.7, 249.1 m^2/g of TAPT–OCH_3, TAPB–OCH_3, and TAPA–OCH_3, respectively. Corresponding pore size distributions were 3.01, 2.63, and 1.19 nm, confirming the mesoporous nature of these frameworks for oxygen adsorption and water diffusion. The denser molecular stacking in the latter two frameworks resulted in smoother surfaces and reduced specific surface areas, consistent with the BET surface area measurements. The contact angle measurements for the synthesized COFs were conducted to evaluate their surface hydrophilicity (Fig.

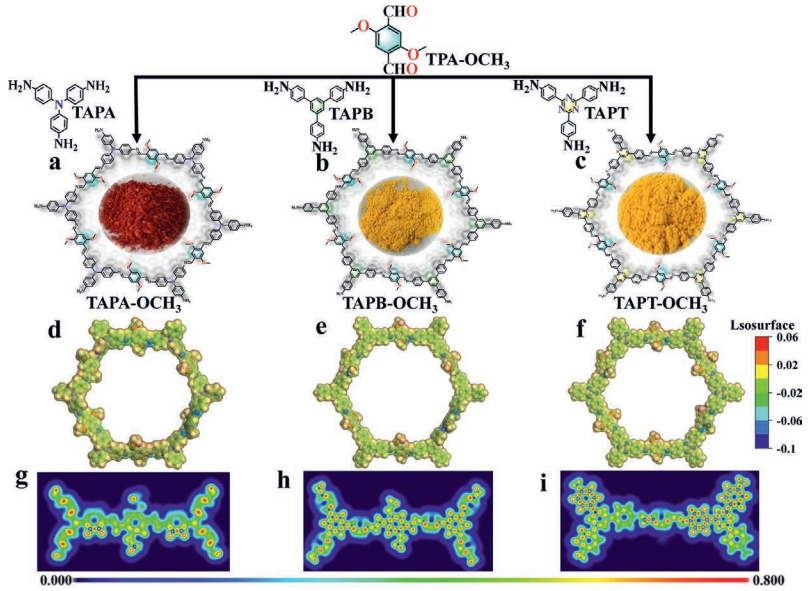


Fig. 1. (a-c) Schematic diagrams. (d-f) Electrostatic potential maps models. (g-i) LOL-π isosurfaces of the obtained COFs.

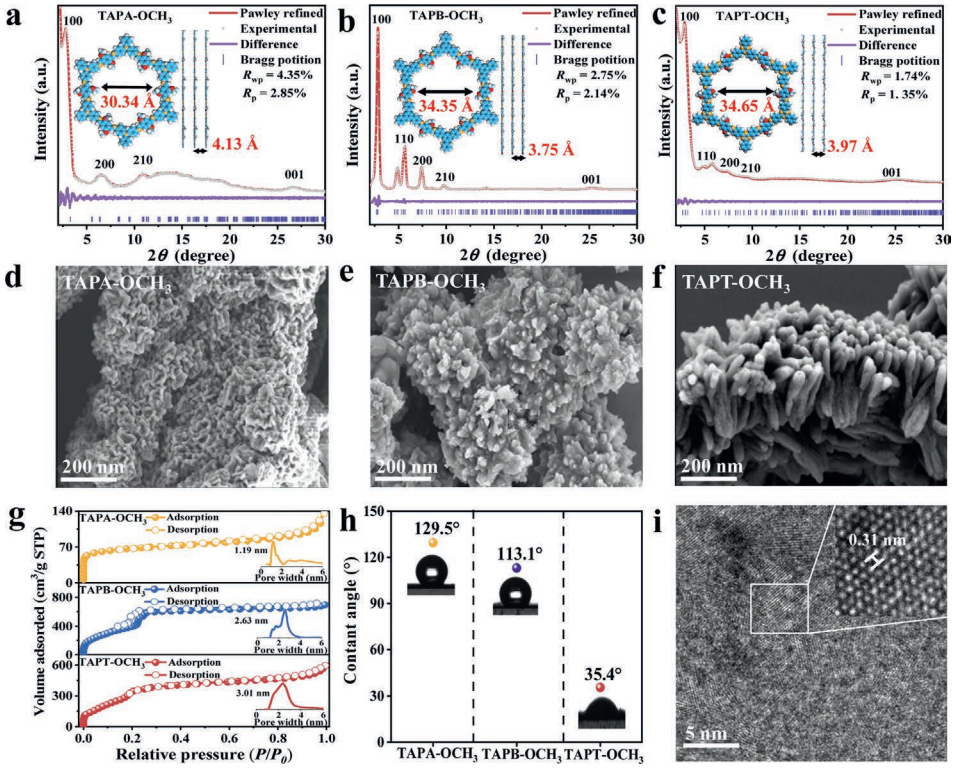


Fig. 2. (a-c) PXRD patterns with the top and side view of corresponding simulated packing structures. (d-f) SEM images. (g) N_2 sorption isotherms with calculated pore size distributions. (h) The contact angle for the synthesized COFs. (i) TEM image of TAPT–OCH_3.

2h). In contrast to TAPB–OCH_3 and TAPA–OCH_3 (>95°), TAPT–OCH_3 showed a notably smaller contact angle (35.4°), suggesting a slight improvement in water affinity upon incorporating the more polar triazine core into the TAPT–OCH_3 framework. As shown in (Fig. 2i), TAPT–OCH_3 displayed a clear honeycomb-like porous structure of *ca.* 0.31 nm, in accordance with the in-plane pore channels in the proposed AA-stacked structure. The highly ordered spatial arrangements with well-defined chemical structures in TAPT–OCH_3 are critical for understanding the structure-activity property relationship of porous organic semiconductors.

The structural integrity of the synthesized COFs was verified through Fourier-transform infrared (FT-IR) spectra and ^{13}C solid-state nuclear magnetic resonance (^{13}C NMR). As shown in Fig. 3a, the FT-IR spectra exhibited a characteristic imine bond (C=N) vibration peak at 1579 cm^{-1}, alongside triazine ring-associated signals at 1512, 1360, and 812 cm^{-1}, confirms the formation of imine linkages *via* Schiff-base condensation [35]. Additionally, the absence of the C=O stretching band (1035 cm^{-1}) from the TAP–OCH_3 monomer and the diminished intensity of N–H stretching bands (3360 cm^{-1}) from TAPT monomers (Fig. S3 in Supporting informa-

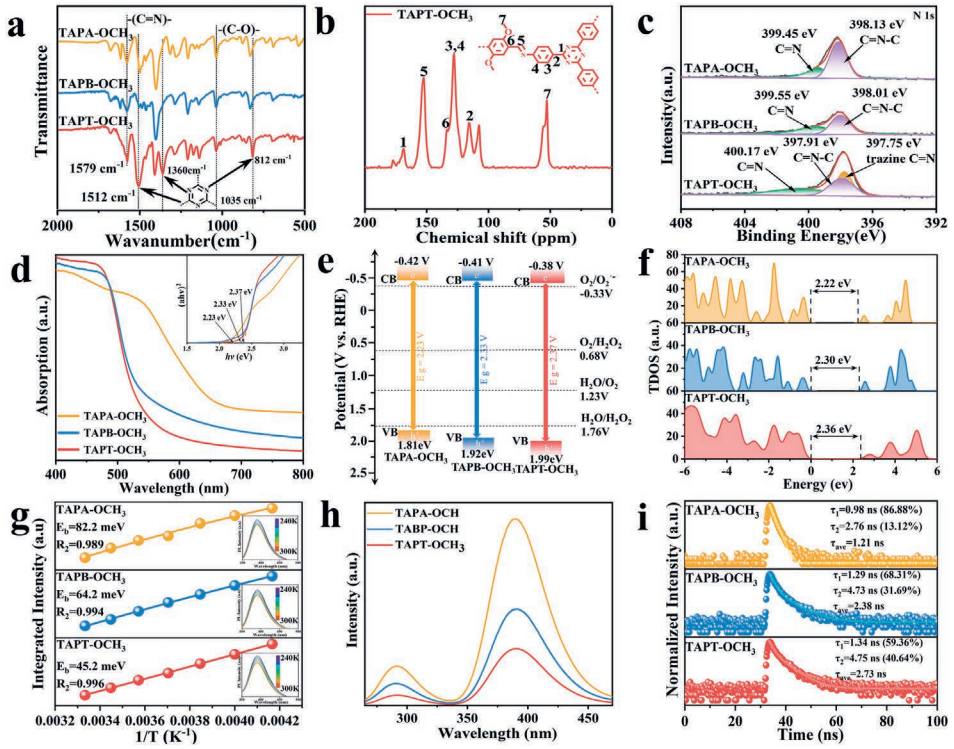


Fig. 3. (a) FT-IR spectra, (b) ^{13}C NMR spectra, (c) XPS spectra of N 1s, (d) UV–vis DRS spectra, (e) calculated band alignments, (f) the calculated TDOS, (g) temperature-dependent PL spectral, (h) steady-state PL spectra, (i) time-resolved PL spectra of synthesized COFs.

tion) confirm the complete polymerization of TAPT–OCH_3. Complementing these findings, the ^{13}C NMR spectra (Fig. 3b) displayed a resonance at 152 ppm, consistent with C=N bond formation, and a peak at 168 ppm corresponding to triazine ring carbons [36]. Elemental composition and bonding configurations were further corroborated by X-ray photoelectron spectroscopy (XPS). The high-resolution N 1s spectrum of TAPT–OCH_3 (Fig. 3c) revealed two peaks at 397.91 and 400.17 eV, assigned to C=N-C and C=N bonds, respectively, Meanwhile, peaks at around 397.75 eV can be assigned to the sp^2 hybridized -C=N- in triazine ring [37]. Notably, the C 1s binding energy of TAPT–OCH_3 shifted higher (Fig. S4 in Supporting information), while the N 1s energy shifted lower compared to TAPB–OCH_3 and TAPA–OCH_3. These trends align with the anticipated electronic modulation induced by the D-A configuration of C=N bonds, which enhances charge transfer efficiency [38]. The synthesis was highly reproducible, yielding the target COF in an average isolated yield of 85% (±3%) over five separate batches, with uniformity confirmed by identical FT-IR spectra (Fig. S5 in Supporting information). Furthermore, the framework demonstrated excellent stability, retaining its structural integrity after 48 h of exposure to various conditions, as confirmed by post-exposure FT-IR analysis (Fig. S6 in Supporting information). This robustness is a critical attribute for its application in photocatalytic systems.

The photocatalytic performance of the synthesized COFs depends critically on their light absorption capabilities and electronic band structure [39]. As shown in Fig. 3d, all COFs displayed strong visible-light absorption, with optical bandgaps of 2.23 eV for TAPA–OCH_3, 2.33 eV for TAPB–OCH_3, and 2.37 eV for TAPT–OCH_3. Critically, reported data indicate that differences in visible-light absorption alone cannot account for the significant variations in H_2O_2 production efficiency observed among these materials [40]. Mott-Schottky measurements (Fig. 3e and Fig. S7 in Supporting information) revealed that the conduction band potentials of all COFs were sufficiently negative to drive oxygen reduction to H_2O_2, while their valence band potentials were sufficiently positive to enable water oxidation, thermodynamically enabling photocatalytic H_2O_2 generation. Considering partial density of states (PDOS), further analysis revealed that TAPT–OCH_3 exhibits smaller bandgaps near the Fermi level compared to TAPA–OCH_3 and TAPB–OCH_3 (Fig. 3f), suggesting improved electron mobility and conductivity. To evaluate charge transfer dynamics, electrochemical impedance spectroscopy and photocurrent response measurements were performed. TAPT–OCH_3 demonstrated the smallest semicircle radius in Nyquist plots (Fig. S8 in Supporting information) and the highest photocurrent density (Fig. S9 in Supporting information), reflecting its superior charge separation efficiency and reduced interfacial resistance.

Temperature-dependent photoluminescence (TD-PL) studies provided insights into exciton behavior: the full-width at half-maximum of PL spectra broadened (Fig. 3g) as temperatures decreased from 300 K to 240 K. Using the Arrhenius equation, the E_b value of TAPT–OCH_3 was calculated as 45.2 meV, significantly lower than those of TAPB–OCH_3 (64.2 meV) and TAPA–OCH_3 (82.2 meV). This lower E_b suggests that TAPT–OCH_3 facilitates easier exciton dissociation into free charges, likely due to its rotation-inhibited π-conjugated structure. Steady-state PL spectra (Fig. 3h) showed weaker emission intensity for TAPT–OCH_3, implying reduced electron-hole recombination, a feature attributed to its D-π-A configuration. Time-resolved PL decay analysis (Fig. 3i) further revealed prolonged charge carrier lifetimes in TAPT–OCH_3, allowing greater participation of photogenerated charges in catalytic reactions. Collectively, these findings highlight optimized photophysical and electrochemical properties of TAPT–OCH_3, which minimize energy loss and electron recombination, ultimately improving photocatalytic efficiency.

The photocatalytic performance for H_2O_2 generation was evaluated in pure water without sacrificial agent. As shown in Fig. 4a, TAPT–OCH_3 demonstrated a steady increase in H_2O_2 accumulation upon visible-light irradiation (λ >420 nm), reaching a production rate of 924.1 μmol g^{-1} h^{-1}. This performance surpassed that

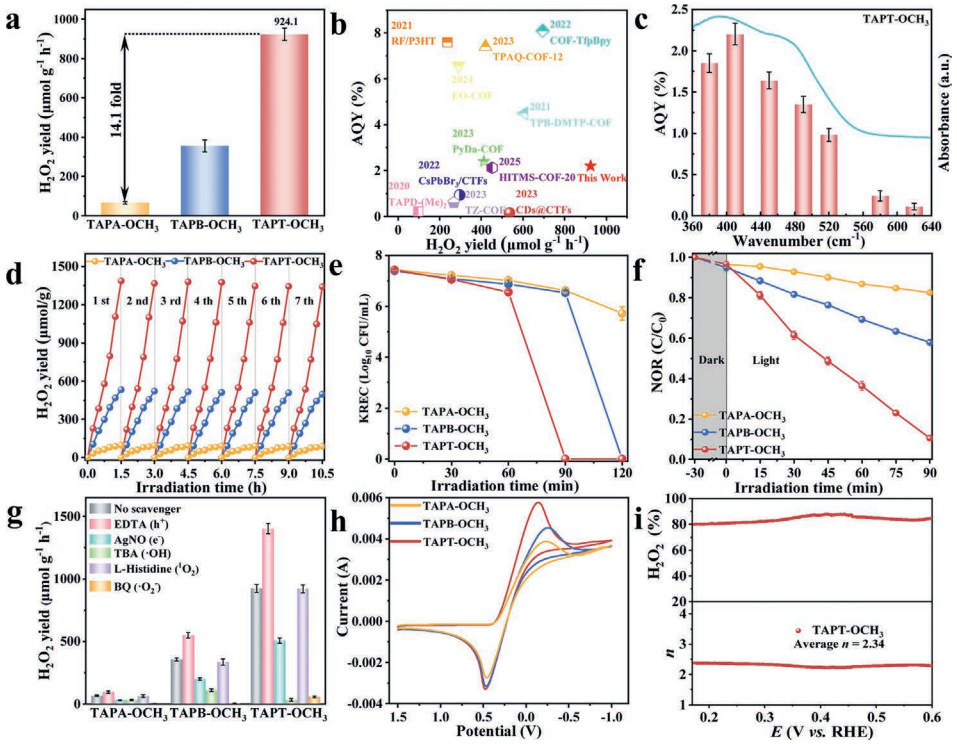


Fig. 4. (a) Time course of photocatalytic H_2O_2 production. (b) Performance comparison with reported photocatalysts. (c) Wavelength-dependent AQY values and solid-state UV-visible spectrum. (d) Cycling stability tests. (e) Bacterial inactivation. (f) Pollutants degradation. (g) Photoactivity in the presence of different scavengers. (h) CV test. (i) RRDE analysis for electron transfer number and H_2O_2 selectivity.

of TAPB–OCH_3 by 2.6-fold (355.5 μmol g^{-1} h^{-1}) and TAPA–OCH_3 by 14.1-fold (65.24 μmol g^{-1} h^{-1}) under identical conditions, underscoring the superior efficiency imparted by the triazine linkage in TAPT–OCH_3. Remarkably, even TAPT–OCH_3 outperformed many previously reported COF-based photocatalysts under comparable conditions, achieving this high efficiency without the use of any sacrificial agents, which highlights its superior intrinsic activity for photocatalytic H_2O_2 production (Fig. 4b and Table S2 in Supporting information). Consistent with its strong visible-light absorption, TAPT–OCH_3 achieved an apparent quantum yield (AQY) of 2.21 % at 420 nm, with diminishing yields at longer wavelengths (Fig. 4c). Moreover, its solar-to-chemical efficiency of 0.23 % also exceeded many existing COF systems, positioning it as a leading photocatalyst for H_2O_2 production. Critically, TAPT–OCH_3 retained full photocatalytic activity and structural stability over seven consecutive cycles (Fig. 4d), with minimal H_2O_2 decomposition observed during irradiation (Fig. S10 in Supporting information), highlighting its potential for long-term use. Post-reaction PXRD (Figs. S11a–c in Supporting information) and FT-IR (Figs. S11d–f in Supporting information) analyses confirm the robust structural integrity of TAPT–OCH_3, whose high activity and long-term stability make it a leading candidate for sustainable photocatalytic H_2O_2 production.

To enable practical application, TAPT–OCH_3 powders were integrated into a continuous-flow reactor, maintaining a stable H_2O_2 generation rate of 716 μmol g^{-1} h^{-1} over 20 h of visible-light exposure (Figs. S12a and b in Supporting information) [41,42]. The generated H_2O_2 demonstrated efficacy in real-world applications: The filtrate from TAPT–OCH_3 effectively neutralized antibiotic-resistant bacteria in dark conditions (Fig. S13 in Supporting information), while the material itself enabled *in-situ* bacterial inactivation (Fig. 4e) and degradation of pollutants such as norfloxacin under visible light (Fig. 4f). To exclude the potential role of reactive chlorine species (RCS), a control test in PBS buffer showed nearly identical disinfection kinetics to those in NaCl solution (Figs. S14a–c in Supporting information), confirming that bactericidal activity originates primarily from material-derived ROS rather than RCS. Quenching assays with various scavengers (Fig. S15 in Supporting information) identified ·OH as the primary ROS responsible for bacterial inactivation, based on significantly reduced efficacy upon adding TBA (·OH scavenger) [43]. The similar inhibition by methanol (scavenges ·OH and ·Cl) and lack of enhancement with high NaCl concentration jointly confirm that ·Cl plays a negligible role. Notably, H_2O_2 production remained robust across a broad pH range (3–11; Fig. S16 in Supporting information) and in diverse water matrices, including tap, river, and seawater, with rates exceeding 880 μmol g^{-1} h^{-1} (Fig. S17 in Supporting information). Catalytic tests in water with various common ions (K^+, Mg^{2+}, Ca^{2+}, Zn^{2+}, Cl^-, HCO_3^-, CO_3^{2-}, SO_3^{2-}, HPO_4^{2-}, NO_3^-) show a maintained high H_2O_2 production rate (>850 μmol g^{-1} h^{-1}), demonstrating remarkable tolerance to common ions (Figs. S18a and b in Supporting information). Additionally, the material maintained excellent photocatalytic H_2O_2 production performance after 12–48 h of ultraviolet light exposure and with the addition of calcium carbonate (5–20 mmol/L) as simulated dirt (Fig. S19 in Supporting information), demonstrating high durability. Collectively, these results highlight TAPT–OCH_3 as a stable, efficient, and adaptable materials for advanced water purification and environmental remediation technologies.

To clarify the reaction pathways underlying H_2O_2 photosynthesis, control experiments were performed under varying gas atmospheres and scavenger conditions. As illustrated in Fig. 4g, introducing an electron scavenger ($AgNO_3$) under N_2-saturation caused a slight reduction in H_2O_2 yield, suggesting that both the $2e^-$ ORR and $1e^-$ WOR pathways drive H_2O_2 photosynthesis in TAPT–OCH_3 system. Meanwhile, the absence of detectable O_2 in water oxidation experiments further ruled out the involvement of $4e^-$ WOR in the H_2O_2 photosynthesis process by TAPT–OCH_3 (Fig. S20 in Supporting information). Further insights into the reaction mech-

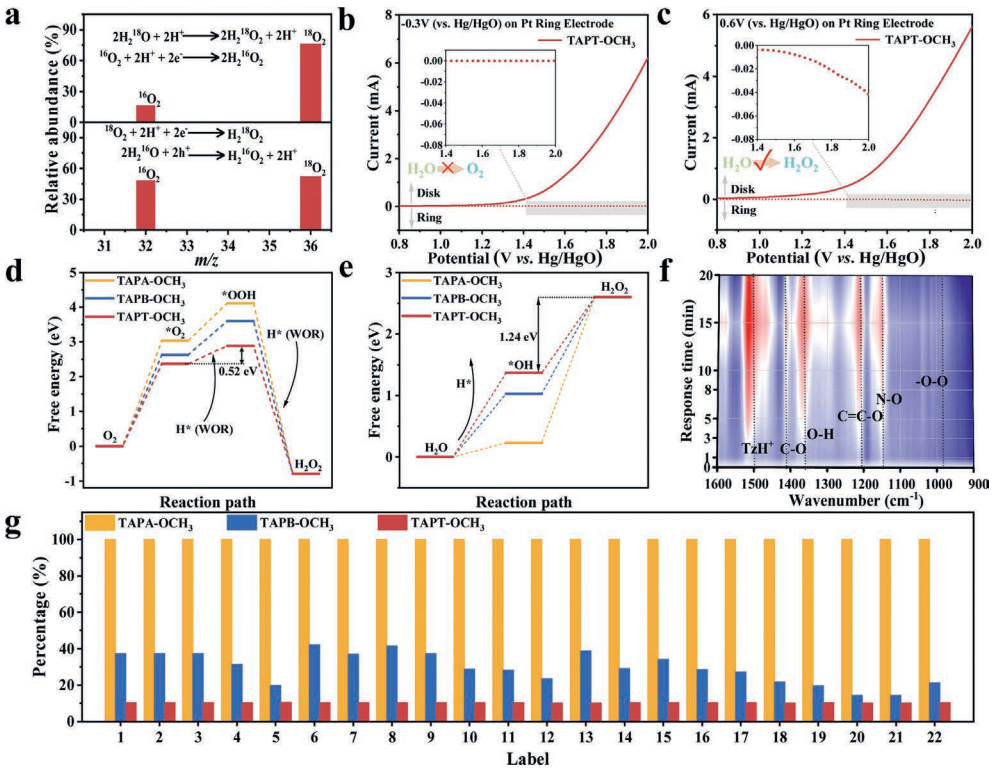


Fig. 5. (a) $H_2{}^{18}O$ and $^{18}O_2$ isotope labeling experiment. RRDE voltammograms set at (b) −0.3 V *vs.* Ag/AgCl to detect O_2 and set at (c) 0.6 V *vs.* Ag/AgCl to detect H_2O_2. Calculated energy profile for (d) reduction of oxygen into H_2O_2 and (e) oxidation of water into H_2O_2. (f) *In-situ* DRIFT spectra of TAPT–OCH_3 during H_2O_2 generation under light irradiation. (g) Life cycle assessment label: 1-Global warming, Human health; 2-Global warming, Terrestrial ecosystems; 3-Global warming, Freshwater ecosystems; 4-Stratospheric ozone depletion; 5-Ionizing radiation; 6-Ozone formation, Human health; 7-Fine particulate matter formation; 8-Ozone formation, Terrestrial ecosystems; 9-Terrestrial acidification; 10-Freshwater eutrophication; 11-Marine eutrophication; 12-Terrestrial ecotoxicity; 13-Freshwater ecotoxicity; 14-Marine ecotoxicity; 15-Human carcinogenic toxicity; 16-Human non-carcinogenic toxicity; 17-Land use; 18-Mineral resource scarcity; 19-Fossil resource scarcity; 20-Water consumption, Human health; 21-Water consumption, Terrestrial ecosystem; 22-Water consumption, Aquatic ecosystems.

anism were obtained using *p*-benzoquinone (*p*-BQ) as a scavenger for superoxide radicals ($O_2^{\bullet-}$) [44]. The significant decline in H_2O_2 production upon adding *p*-BQ highlighted $O_2^{\bullet-}$ as a key intermediate. This finding was corroborated by electron spin resonance (ESR) spectroscopy, which detected DMPO–$O_2^{\bullet-}$ signals under visible light (Fig. S21a in Supporting information), and nitroblue tetrazolium (NBT) assays, which quantitatively confirmed $O_2^{\bullet-}$ presence (Fig. S21b in Supporting information). Cyclic voltammetry (CV) in an O_2-saturated environment revealed a prominent oxygen reduction peak at −0.23 V *vs.* RHE for TAPT–OCH_3 (Fig. 4h), indicating strong oxygen reduction activity with low energy demand. Rotating ring-disk electrode (RRDE) analysis further supported this, showing an average electron transfer number of 2.34 and a H_2O_2 selectivity of 82 % ± 2 % (Fig. 4i). Together, these results confirm that H_2O_2 generation in TAPT–OCH_3 system proceeds *via* a two-step indirect ORR mechanism, where O_2 is first reduced to $O_2^{\bullet-}$, followed by its subsequent conversion to H_2O_2.

To elucidate the mechanism of H_2O_2 generation *via* 1e⁻ WOR, $^{\bullet}$OH trapping experiments were conducted using *t*–butyl alcohol (TBA) under N_2 atmosphere. As shown in Fig. 4g, the addition of TBA resulted in a slight reduction in H_2O_2 yield, suggesting that $^{\bullet}$OH contributes to the photocatalytic H_2O_2 production in the TAPT–OCH_3 system. This observation aligns with the DMPO-$^{\bullet}$OH signals detected in EPR spectra (Fig. S22 in Supporting information). Further isotopic experiments employing $H_2{}^{18}O$ and $^{18}O_2$ confirmed that H_2O_2 originates directly from the ORR and WOR by TAPT–OCH_3 (Fig. 5a). Electrochemical analyses provided additional insights into the reaction pathway. Under N_2 atmosphere, the ring electrode potential was fixed at −0.3 V (*vs.* Ag/AgCl) to monitor oxygen evolution. The absence of detectable ring current for TAPT–OCH_3 (Fig. 5b) rules out a 4e⁻ WOR pathway. Conversely, when the ring electrode was set to the H_2O_2 oxidation potential (0.6 V *vs.* Ag/AgCl), a distinct oxidation current emerged (Fig. 5c), confirming H_2O_2 generation *via* the 1e⁻ WOR process. These results corroborate the $^{\bullet}$OH quenching experiments, solidifying the dominance of the 1e⁻ WOR pathway. Accordingly, the proposed mechanism involves exciton dissociation in TAPT–OCH_3 under light irradiation, generating photogenerated e^--h^+ pairs. The photogenerated e^- reduce oxygen to form $O_2^{\bullet-}$, and subsequently converted to H_2O_2, while the h^+ oxidize water to adsorbed $^{\bullet}$OH, which then combine to yield H_2O_2. These results provide solid support that TAPT–OCH_3 undergo the 2e⁻ ORR process on H_2O_2 production, whereas a 1e⁻ WOR demonstrates remarkably enhanced overall photocatalytic activity.

To elucidate the photocatalytic mechanism underlying H_2O_2 generation, first-principles calculations were performed. For the 2e⁻ ORR process, TAPT–OCH_3 exhibited a smaller energy barrier during the initial $^*O_2$ formation step and a substantially reduced Gibbs free energy difference (ΔG) for the rate-determining *OOH intermediate than TAPA–OCH_3 and TAPB–OCH_3 (Fig. 5d and Fig. S23 in Supporting information). These results highlight superior oxygen affinity and catalytic efficiency of TAPT–OCH_3 in facilitating ORR. Regarding the WOR step, the ΔG of *OH adsorption on TAPT–OCH_3 was found to be optimal for H_2O_2 production (Fig. 5e and Fig. S24 in Supporting information). Excessively strong *OH adsorption could trigger over-oxidation to O_2, while weaker adsorption would release free $^{\bullet}$OH, both detrimental to selective H_2O_2 production [39,41]. Notably, TAPT–OCH_3 demonstrated a low energy barrier (0.52 eV) for the critical $^*OOH \rightarrow H_2O_2$ step but higher barriers for further oxidation to $^*O$ (2.06 eV) or *OH (1.24 eV), fa-

voring selective $2e^-$ oxidation over competing $4e^-$ pathways. Complementary *in-situ* diffuse reflectance infrared Fourier transform spectroscopy (DRIFTS) identified key intermediates and active sites (Fig. 5f). Under light irradiation, the vibration peak at 976 cm^{-1} in TAPT–OCH_3 were assigned to adsorbed peroxy species (-O-O) respectively [45]. Additional peaks of C–O (1410 cm^{-1}) and C=C-O (1213 cm^{-1}) confirmed O_2 reduction at C atoms of TAPT–OCH_3. During water oxidation, intensified peaks at 1150 cm^{-1} (N–O) and 1367 cm^{-1} (O–H), along with the emergence of TzH^+ 1518 cm^{-1}, indicating that the water oxidation surrounding the N atoms in triazine rings of TAPT–OCH_3 [39]. Accordingly, its coplanar π-conjugated structure of TAPT–OCH_3 enhances exciton dissociation, yielding abundant charge carriers. Photoexcited electrons drive sequential O_2 reduction *via* $^*O_2^-$ intermediates, while holes oxidize water through $^*OH$ species, sustaining the photocatalytic cycle for H_2O_2 synthesis.

Life cycle assessment (LCA) is critical for evaluating the environmental sustainability of the obtained COFs and informing strategies to align their development with global sustainability goals [46]. Using experimental data, the LCA checklists for the three COF synthesis were established in Tables S3-S5 (Supporting information). A range of descriptive indicators pertinent to wastewater treatment processes were employed in Fig. 5g, such as global warming, stratospheric ozone depletion and human carcinogenic toxicity, which helps us comprehensively evaluate the stability applications [47]. Further analysis using the endpoint ReCiPe methodology (Text S6) quantified impacts on human health, ecosystems, and resource depletion [48]. Toxicity effects (indicators 12–16) cover human carcinogenic, non-carcinogenic, and ecological toxicity, particularly relevant in systems involving chemicals, industrial processes, or e-waste. Ecosystem quality is assessed *via* eutrophication potential (indicators 10–11), crucial for systems with agricultural activities or wastewater discharge. Water resource impacts (indicators 20–22) apply to water-sensitive or high-consumption systems, evaluating effects on human health and aquatic ecosystems. Resource consumption is captured by mineral and fossil resource scarcity (indicators 18–19), essential for systems dependent on such materials. The results (Fig. S25 in Supporting information) indicated that TAPT–OCH_3 COF exhibit exceptional chemical resilience and reusability, retaining the initial pollutant removal efficiency even after multiple cycles, consistent with the durability long-term material consumption and waste generation, aligning with circular economy principles derived in Fig. 5g. Notably, the TAPT–OCH_3 COF exhibited notably higher environmental impacts, primarily attributed to the lower E_b for exciton dissociation in its rotation-inhibited π-conjugated structure. This trade-off positions it as a promising candidate for practical wastewater treatment despite synthesis challenges.

In summary, we present a straightforward yet impactful strategy to enhance photocatalytic H_2O_2 production by optimizing the coplanar structure of the TAPT–OCH_3 COF. Through detailed analysis of the methoxy–triazine-modified TAPT–OCH_3, we demonstrated that this design promotes exciton dissociation and improves charge-carrier separation and migration. The system also achieved a solar-to-chemical conversion efficiency of 0.23 % and an apparent quantum yield of 2.21 % at 420 nm using only water and oxygen under simulated sunlight, surpassing current benchmarks for metal-free photocatalysts. The enhanced activity stems from the extended D-A units within the two-dimensional framework, which simultaneously optimizes the $2e^-$ ORR and $1e^-$ WOR pathways. This dual improvement ensures atom utilization efficiency, enabling highly efficient overall H_2O_2 photosynthesis. Our findings pave the way for developing sustainable, high-performance metal-free materials for green H_2O_2 production and other energy conversion applications.

Declaration of competing interest

The authors declare that they have no known competing financial interests or personal relationships that could have appeared to influence the work reported in this paper.

CRediT authorship contribution statement

Jun Gao: Writing – original draft, Investigation, Formal analysis, Data curation, Conceptualization. **Lichao Wang:** Formal analysis, Data curation, Conceptualization. **Shunwei Huang:** Supervision, Software, Data curation. **Hao Du:** Software, Formal analysis, Data curation. **Huayue Zhu:** Supervision, Software. **Derek Hao:** Validation, Supervision, Software. **Yanling Wu:** Methodology, Investigation, Formal analysis. **Qi Wang:** Writing – review & editing, Funding acquisition, Formal analysis, Conceptualization. **Limin Jin:** Writing – review & editing, Writing – original draft, Supervision, Data curation, Conceptualization.

Acknowledgments

This work was supported by “Pioneer” and “Leading Goose” R&D Program of Zhejiang (No. 2025C02240), National Natural Science Foundation of China (No. 22276168).

Supplementary materials

Supplementary material associated with this article can be found, in the online version, at doi:10.1016/j.cclet.2025.112283.

References

[1] C. Wang, X. Xie, F. Qiu, et al., Chin. Chem. Lett. 37 (2026) 111604.
[2] F.N. Habarugira, D. Yao, W. Miao, et al., Chin. Chem. Lett. 35 (2024) 109886.
[3] L. Li, J. Bai, J. Li, B. Zhou, Chem. Eng. J. 506 (2025) 159828.
[4] J. Li, N. Xu, Y. Zhang, et al., Chin. Chem. Lett. 36 (2025) 110470.
[5] Q. Yang, Y. Zhang, P. Xiao, et al., Environ. Sci. Technol. 58 (2024) 19058–19069.
[6] Y. Liu, J. Li, B. Zhou, et al., Environ. Chem. Lett. 7 (2009) 363–368.
[7] L. Jin, J. Xu, H. Zhu, et al., Chin. Chem. Lett. (2025), doi:10.1016/j.cclet.2025.111865.
[8] C. Zhang, W. Shen, K. Guo, et al., J. Am. Chem. Soc. 145 (2023) 11589–11598.
[9] T. Huang, W. Zhang, S. Yang, et al., Smart Mat. 5 (2024) e1309.
[10] J.Y. Yue, L.P. Song, Y.F. Fan, et al., Angew. Chem. Int. Ed. 62 (2023) e202309624.
[11] L. Jin, M. Deng, J. Gao, et al., Chem. Eng. J. 515 (2025) 163722.
[12] Q. Li, M. Deng, J. Gao, et al., Sep. Purif. Technol. 362 (2025) 131722.
[13] L. Wang, H. Du, X. Wang, et al., Environ. Res. 272 (2025) 121166.
[14] L.M. Jin, M. Sun, J.P. Yang, et al., Appl. Catal. B: Environ. 339 (2023) 123150.
[15] R. Wang, J. Liu, Q. Zhang, et al., Water Res. 252 (2024) 121209.
[16] J. Zhang, Z. Zhou, Z. Feng, et al., Environ. Sci. Technol. 56 (2022) 1331–1340.
[17] L. Jin, Y. Wang, Q. Li, et al., Appl. Catal. B: Environ. 373 (2025) 125328.
[18] X. Lu, Y. Chang, S. Wang, et al., Chin. Chem. Lett. 36 (2025) 110277.
[19] S.K. Loeb, P.J.J. Alvarez, J.A. Brame, et al., Environ. Sci. Technol. 53 (2019) 2937–2947.
[20] M.Y. Sun, L. Zhang, Y. Li, et al., Chin. Chem. Lett. 36 (2025) 110035.
[21] Z. Teng, H. Yang, Q. Zhang, et al., Nat. Chem. 16 (2024) 1250–1260.
[22] X.X. Wang, C.R. Zhang, R.X. Bi, et al., Adv. Funct. Mater. 35 (2025) 2421623.
[23] L. Wang, D. Ma, A. Liu, et al., Angew. Chem. Int. Ed. 64 (2025) e202518097.
[24] H. Li, R. Chen, L. Sun, et al., Adv. Mater. 36 (2024) 2408778.
[25] S. Li, S. Xu, E. Lin, et al., Nat. Chem. 17 (2025) 226–232.
[26] A. Dey, F.A. Rahimi, S. Barman, et al., J. Mater. Chem. A 11 (2023) 13615–13622.
[27] X. Wang, H. Li, S. Zhou, et al., Adv. Funct. Mater. 35 (2025) 2424035.
[28] R.J. Wei, X. Luo, G.H. Ning, D. Li, Acc. Chem. Res. 58 (2025) 746–761.
[29] H. Yan, M. Shen, Y. Shen, et al., Proc. Natl. Acad. Sci. U. S. A. 119 (2022) e2202913119.
[30] H. Chen, D. Li, M. Lin, et al., Adv. Mater. 37 (2025) 2500063.
[31] T. Ma, L. Wei, L. Liang, et al., Nat. Commun. 11 (2020) 6128.
[32] J. He, H. Liu, F. Zhang, et al., Adv. Funct. Mater. 32 (2022) 2110030.
[33] X. Zhang, S. Cheng, C. Chen, et al., Nat. Commun. 15 (2024) 2649.
[34] Z. Chen, B. Yang, J. Li, et al., Chin. Chem. Lett. 36 (2025) 110320.
[35] L. Zhang, C. Wang, Q. Jiang, et al., J. Am. Chem. Soc. 146 (2024) 29943–29954.
[36] W. Zeng, Y. Dong, X. Ye, et al., Chin. Chem. Lett. 35 (2024) 109252.
[37] Y. Yang, H. Niu, L. Xu, et al., Appl. Catal. B: Environ. 269 (2020) 118799.
[38] X. Chen, X. Zhang, X. Xiao, et al., Angew. Chem. Int. Ed. 62 (2023) e202216010.
[39] F. Liu, P. Zhou, Y. Hou, et al., Nat. Commun. 14 (2023) 4344.
[40] C. Qin, X. Wu, L. Tang, et al., Nat. Commun. 14 (2023) 5238.

[41] M. Xie, W. Zheng, M. Sun, et al., Appl. Catal. B 345 (2024) 123708.
[42] B. Shen, H. Du, A. Liu, et al., J. Clean Prod. 523 (2025) 146458.
[43] A. Liu, X. Ma, B. Shen, et al., Chem. Eng. J. 504 (2025) 158929.
[44] S. Chen, J. Gao, P. Wang, et al., Sep. Purif. Technol. 378 (2025) 134672.
[45] C. Yang, L. Hou, J. Yang, et al., Chem. Eng. J. 510 (2025) 161631.
[46] G. Ren, J. Zhang, T. Rao, et al., Appl. Catal. B: Environ. 373 (2025) 125349.
[47] Y. Ren, J. Wang, L. Yang, et al., Environ. Sci. Technol. 59 (2025) 11414–11425.
[48] E. Chatzisymeon, S. Foteinis, D. Mantzavinos, T. Tsoutsos, J. Clean Prod. 54 (2013) 229–234.